International Journal of ENGINE RESEARCH

Standard Article

International J of Engine Research
1–18

DOI: 10.1177/1468087420985189
journals.sagepub.com/home/jer
SAGE

Numerical simulation of fuel dribbling and nozzle wall wetting

Manolis Gavaises[1], Mithun Murali-Girija[1], Carlos Rodriguez[1], Phoevos Koukouvinis[1], Martin Gold[2] and Richard Pearson[2]

Abstract

The present work describes a numerical methodology and its experimental validation of the flow development inside and outside of the orifices during a pilot injection, dwelt time and the subsequent start of injection cycle. The compressible Navier-Stokes equations are numerically solved in a six-hole injector imposing realistic conditions of the needle valve movement and considering in addition a time-dependent eccentric motion. The valve motion is simulated using the immersed boundary method; this allows for simulations to be performed at zero lift during the dwelt time between successive injections, where the needle remains closed. Moreover, the numerical model utilises a fully compressible two-phase (liquid, vapour) two-component (fuel, air) barotropic model. The air's motion is simulated with an additional transport equation coupled with the VOF interface capturing method able to resolve the near-nozzle atomisation and the resulting impact of the injected liquid on the oleophilic nozzle wall surfaces. The eccentric needle motion is found to be responsible for the formation of strong swirling flows inside the orifices, which not only contributes to the breakup of the injected liquid jet into ligaments but also to their backwards motion towards the external wall surface of the injector. Model predictions suggest that such nozzle wall wetting phenomena are more pronounced during the closing period of the valve and the re-opening of the nozzle, due to the residual gases trapped inside the nozzle, and which contribute to the poor atomisation of the injected fluid upon re-opening of the needle valve in subsequent injection events.

Keywords

Cavitation, fuel dribbling, wall-wetting, fuel injectors

Date received: 15 June 2020; accepted: 6 November 2020

Introduction

The level of emissions from internal combustion engines (ICE) has perplexed the relative industries for past few decades; the well-known soot-NO_X trade off pauses a difficult problem for the simultaneous reduction of these pollutants; see selectively[1,2] among many others. The advancements in ICE technology that have brought pollutant levels down a 1000-fold in past decades[3] now make particulate emissions from tire and brake wear a larger problem than engine emissions for both IC engine powered and electric vehicles. Today's emission issues are mainly related to insufficient oxygen due to local improper mixing, nozzle and piston wall wetting and fuel dribbling at the end of injection. Dribbling and wall wetting can lead to accumulation of carbonaceous deposit formation on the internal and external walls of an injector resulting to increased emissions.[4,5]

Tremendous efforts have been made in the past three decades to study the flow inside and in the vicinity of the nozzle holes of diesel injectors both experimentally and numerically, as this is the key for further reduction of emissions. Overall, remarkable improvements in injection strategies, such as increasing the injection pressure to a range of 3000 bars,[6] controlling the injection-rate shaping and timing the injection,[7] split or multiple injections[8,9] and improved orifice geometry and orientation[10] are now standard practices. Numerical simulations have shed light to the effect on multi-phase flow development in various nozzle configurations, see for example,[11–17] while more recent

[1]School of Mathematics, Computer Science and Engineering, City, University of London, London, UK
[2]BP International Ltd, London, UK

Corresponding author:
Manolis Gavaises, School of Mathematics, Computer Science and Engineering, City, University of London, Northampton Square, London, EC1V 0HB, UK.
Email: M.Gavaises@city.ac.uk

investigation have quantified the needle valve motion using high energy X-rays[18–22] and real size optical nozzles.[23–26] Still, the flow phenomena taking place during the very short time scales ($\sim 100\mu s$) of the opening and closing of the needle valve controlling the injection process are challenging to be quantified. In particular, fuel dribbling, which is the formation of poorly atomised unintended fuel jet after the closure of the needle valve is poorly understood.

High-speed Mie-scattering and shadowgraphy imaging techniques[27] studied the liquid-phase penetration and vapourisation during quasi-steady and transient conditions realised after EOI. They found that the liquid penetration length decreases after the EOI compared to quasi-steady conditions due to the reduction in mass flow rate. They also formulated a one-dimensional model to explain the formation of entrainment waves from the nozzle towards the jet after the needle valve closure. The formation of this wave was also observed in Kook et al.[28], Musculus;[29] the liquid jet was found to reside towards the injector. In Eagle and Musculus[30] utilised high-speed digital cinematography to observe the spatial and temporal evolution of the dribble after the EOI. They identified three main types of dribble formation; immediate dribble, late-cycle dribble and blow-down dribble. They also discussed the effect of different parameters such as nozzle geometry, fuel type, ambient pressure and temperature, rail pressure, injection schedules on dribble formation. In Moon et al.[31] used X-ray phase-contrast imaging technique to study the needle dynamics and in- and near-nozzle flow characteristics associated with fuel dribble of a three-hole mini-sac type injector. They observed high shot-to-shot variations in dribble formation from the injector hole and inconsistent air ingestion which they attributed to the hole-to-hole flow variations. Two modes of dribbling process were reported, one with a faster breakup and short residence time, and the other one with a large residence time where the dripping of undistributed liquid columns is observed. It was concluded that there is a strong connection between ingested air and dribble formation and the major factor that influence the dribble formation is the needle closure velocity. In a recent study, the tip wetting from a gasoline direct injection nozzle was experimentally evaluated in Hélie et al.,[32] while a novel 3D reconstruction algorithm for predicting the volume of the ligaments formed after end of injection was developed in Sechenyh et al.[33]

So far, dribble formation from an injector nozzle has mainly been studied experimentally and only a few studies have included simulations. In Battistoni et al.[34] studied this process from a single-hole injector using a two-phase three-components mixture model to simulate cavitation while considering the presence of non-condensable gas. They used a Cartesian cut-cell grid generated during run time to incorporate the needle motion. To model the needle closure, they switched to two disconnected domains when the needle lift drops below $10\mu m$; the simulation is continued for $3000\mu s$ to cover the relevant flow dynamics. They observed the formation of cavitation inside the nozzle's sac volume due to sudden pressure drop when the needle valve closes, and the pressure recovery caused by the pullback of the liquid into the nozzle reabsorbs the vapour. In Papadopoulos and Aleiferis,[26] the authors utilised the volume of fluid (VOF) approach with a $k-\omega-SST$ turbulence model to study the full injection process of a real size multi-hole injector. To seal the high-pressure zone from the low-pressure zone at needle closure, they modelled an interface which acts as a 'wall' when the needle lift is below $0.5\mu m$ and as an 'interior' all other times. They observed dripping of fuel from the nozzle after EOI with the nozzle almost filled with liquid fuel when the outlet pressure was set to $60bar$. Whereas at 1 bar outlet pressure, the fuel was almost emptied from the nozzle replaced by the air from the combustion chamber. Since their primary objective was to study the in-nozzle flow with transient needle motion, the fuel dribble was not studied in detail. More recently, Mouvanal et al.[35] studied the internal nozzle flow and the purging of gas into the sac volume during end of injection. In order to model the needle closure, they employed a technique similar to that of Papadopoulos and Aleiferis.[26] All aforementioned studies have assumed needle closure when the clearance between the needle and the sac wall reaches a specified minimum value in order to avoid discontinuity in the computational domain and to maintain numerical stability. A cut-cell based remeshing approach, implemented in the CONVERGE solver was used for studying the development of flow inside a five-hole diesel injector under the influence of 'on-axis' and 'off-axis' needle motion;[15] a significant impact of the needle off-axis motion has been observed at low and medium lifts. The resulting mass flow rate, as well as the liquid jets emerging from the orifices, showed noticeable sensitivity to the needle off-axis motion. A cut-cell based immersed boundary method for modelling the needle motion, without considering the effect of wobble was presented by Örley et al.[16,36] with a primary focus on the developed turbulent structures. Moreover, all aforementioned studies have not considered the compressibility of the phases and they assumed needle motion in the axial direction only. However, the off-axis wobbling motion of the needle is known to produce hole-to-hole flow variation and swirling motion which affects the liquid jet structure during the needle valve opening and closing.[37,38] The recent study of the author's group Gomez Santos et al.[39] is the only that has considered the complete needle valve closure and presented simulations for the flow field after the End of Injection (EOI) considering the compressibility of all phases; still, a sac-type nozzle was simulated while there were no predictions for liquid dribbling.

Several models and approaches exist in the literature for modelling wall-wetting; they typically come under the banner of droplets impact. A detailed review of the phenomena of droplet impact on the solid unheated

and heated surfaces can be found in Jadidbonab et al.[40,41], Strotos.[42,43] Depending on the contact angle between the droplet and the surface, the degree of wettability changes. If the contact angle less than 90° then the surface is favourable for wetting, whereas a contact angle greater than 90° implies that the surface is less favourable for wetting. Recently, some experimental and numerical studies were carried out that focused on the wettability of the nozzle tip and the nozzle plate surface.[44,45] However, a large majority of the numerical studies related to this topic is focused on droplet impact on solid walls. One of the major challenges in numerical modelling of this phenomenon is the implementation of the contact line between the gas-liquid and solid. The most simplistic approach is to specify a static[46] or dynamic[47] contact angle as a boundary condition to which the mean curvature of the surface of the droplets next to the wall will comply. There exist more advanced models that can handle moving interfaces[48] or models that can compute contact angle based on the net of forces acting on the free surface of the droplet on the fly instead of specifying a fixed or temporal evolution of the contact angle.[49]

The present study aims to enhance this important, yet the less explored area of end of injection fuel dribbling from diesel injectors. For this purpose, an implicit VOF model with appropriate treatment for modelling surface tension and wall adhesion is used. A VOF model is used for predicting the liquid-gas interface while the immersed boundary method is used for simulating the moving needle; validation of these models can be found in the previous works of the authors Mithun et al.[11,50,51], Koukouvinis et al.[52] respectively. The results presented here utilise the experimental data from a Delphi DFI 1.3, six-hole VCO nozzle, recently reported by the author's in Gold et al.,[5] in order to validate the current model. At the same time, simulations of the experiments recently presented in Manin et al.[53] are utilised for the first time for further validation of the developed model. This model considers both the in-nozzle and near-nozzle jet simultaneously using a fully compressible two-phase two-component model.[11] The model also considers a predefined axial and eccentric motion of the needle inside the VCO nozzle, using an immersed boundary approach (IBM).[51]

The outline of the paper is as follows. In the next section, the numerical model consisting of the two-phase two-component VOF model, wall adhesion and the IBM used for simulating the needle valve motion are presented. Then a section regarding the limitations of the adopted methodology, the link to previous works and the present contribution is included. This is followed by a description of the problem including the meshing, operating and boundary conditions. After that, the result and discussions for the injection scenarios considered (start of injection, end of injection and the subsequent start of injection) are presented. The major conclusions from the study are highlighted in the final section.

Mathematical model

Governing equation

The fluid flow is governed by the mass and momentum conservation equations. The model assumes a barotropic fluid as the primary phase and non-condensable gas (NCG) as the secondary phase. A Reynolds averaged formulation is used for resolving turbulence. To track the interface between the phases, the continuity equation of the secondary phase (equation (1)) is first solved and then volume fraction of the primary phase is estimated based on the equation (2). The mixture properties such as mixture density and viscosity are then calculated using the mixing rule as given in equations (3) and (4). These properties are then used for the solution of the mixture momentum equation (equation (5)).

$$\frac{\partial(\alpha_g \rho_g)}{\partial t} + \nabla.(\alpha_g \rho_g \bar{u}_g) = 0 \tag{1}$$

$$\alpha_{lv} + \alpha_g = 1 \tag{2}$$

$$\rho_m = (1 - \alpha_g)\rho_{lv} + \alpha_g \rho_g \tag{3}$$

$$\mu_m = (1 - \alpha_g)\mu_{lv} + \alpha_g \mu_g \tag{4}$$

$$\begin{aligned} &\frac{\partial(\rho_m u_i)}{\partial t} + \frac{\partial(\rho_m u_i u_j)}{\partial x_j} = -\frac{\partial p}{\partial x_j} \\ &+ \frac{\partial}{\partial x_j}\left[\mu\left(\frac{\partial u_i}{\partial x_j} + \frac{\partial u_j}{\partial x_i} - \frac{2}{3}\delta_{ij}\frac{\partial u_l}{\partial x_l}\right)\right] \\ &+ \frac{\partial}{\partial x_j}\left(-\rho_m \overline{u_i u_j}\right) + f_\sigma + f_{IB} \end{aligned} \tag{5}$$

where α is the volume fraction, $\dot{m}$ is the mass flow, ρ is the density, μ is the viscosity, u is the velocity, p is the pressure, δ is the Kronecker delta, the subscripts g, m, lv represents the non-condensable gas, mixture, and cavitating fluid respectively. The term $-\rho muiuj$ in equation (5) is the Reynolds stress term, $f\sigma$ is the source term for surface tension force and fIB is the source term for immersed boundary. Turbulence in the flow is modelled using the $k-\omega-SST$ model[54] which has proved to produce good quality results for simulating EOI conditions[26] where the Reynolds number is relatively low. The transport equations solved are given in equations (6) and (7):

$$\frac{\partial}{\partial t}(\rho_m k) + \frac{\partial}{\partial x_i}(\rho_m k u_i) = \frac{\partial}{\partial x_j}\left(\Gamma_k \frac{\partial k}{\partial x_j}\right) + G_k - Y_k + Su_k \tag{6}$$

$$\begin{aligned} \frac{\partial}{\partial t}(\rho_m \omega) + \frac{\partial}{\partial x_j}(\rho_m \omega u_j) &= \frac{\partial}{\partial x_j}\left(\Gamma_\omega \frac{\partial \omega}{\partial x_j}\right) \\ &+ G_\omega - Y_\omega + D_\omega + Su_\omega \end{aligned} \tag{7}$$

where Γ, G, Y are the effective diffusivity, turbulent production and dissipation as defined in Ansys,[55] and Su is the user defined source term. The source terms f_{IB}, Su_k, Su_ω in equations (5)–(7) corresponds to the immersed boundary and its implementation is explained in the following sub-section.

An implicit formulation for the volume of fluid (VOF) approach is used for modelling the two components. The volume fraction equation is discretised using the compressive scheme of Ansys,[55] which is a second-order reconstruction method, with slope limiter values ranging between 0 and 2. A slope limiter value of 2 is used in this study, which corresponds to the CICSAM scheme of Ubbink.[56] The continuum surface force (CSF) approach of Brackbill et al.[47] was used for modelling surface tension which is included as an additional source term ($f\sigma$) to the momentum equations of the VOF model, which is defined as:

$$f_\sigma = \sigma_{ij} \frac{\alpha_m \beta_i \nabla \alpha_i}{\frac{1}{2}(\rho_i + \rho_j)} \tag{8}$$

where β is the curvature of the free surface approximated as:

$$\beta = \nabla . \left(\frac{\nabla \alpha}{|\nabla \alpha|} \right) \tag{9}$$

To model the droplet impingement on a solid surface, the wettability of the wall needs to be accounted for, an approach similar to the one presented in Brackbill et al.[47] is used. The contact angle that the fluid is assumed to make with the wall is used to adjust the surface normal in cells near the wall. The surface normal at the live cell next to the wall $\hat{n}$ is rotated according to the prescribed angle θw (which is assumed as $25o$ in this study) as:

$$\hat{n} = \hat{n}_w cos\theta_w + \hat{n}_t cos\theta_w \tag{10}$$

where $\hat{n}_w$ and n_t are the unit vectors normal and tangent to the wall. The combination of the contact angle and the calculated surface normal on the cell above the wall determines the local curvature of the surface which is used to adjust the surface tension force.

Immersed boundary method

In an IBM, the presence of the body is represented using additional source terms in the governing equations. The IBM formulation used in this study corresponds to the continuous forcing approach,[57] where the source terms are added to the continuous form of governing equations as given in equations (5)–(7). The term fIB in equation (5) is the term that forces the velocity field to follow the geometry boundaries. This force is proportional to the difference between the flow ($\bar{u}$) and target body velocity (UIB) as given in equation (15):

$$f_{IB} = -\frac{{}_m C}{dt} \alpha_{IB} (\bar{u} - \bar{U}_{IB}) \tag{11}$$

In the above equation, the strength of the immersed body velocity is tuned using the term C, which is an arbitrary value, dt is the time step size and α_{IB} is the masking function which takes a value of 1 if the cell is inside the immersed body (solid) and 0 if the cell is outside (fluid). Any value between 0 and 1 refers to a cell which is partially occupied by the wall. For calculating the mask function in each cell, the wall normal distance of each cell nodes from the immersed boundary points is estimated and the IB point with the minimum distance is identified using equaiton (12):

$$d_{n,IB} = (\bar{x}_n - \bar{X}_{IB}).n_{IB}; \quad ifMIN(|\bar{x}_n - \bar{X}_{IB}|) \tag{12}$$

where $\bar{x}_n$ and $\bar{X}_{IB}$ are the coordinates of the cell node and immersed boundary point, n_{IB} is the normal to the wall. The distance from the immersed body to the cell is estimated as the average of node distances equation (13):

$$d_{c,IB} = \frac{\sum_n d_{n,IB}}{n} \tag{13}$$

After estimating the distance function from equation (12), the mask function α_{IB} is calculated using equation (14):

$$\alpha_{IB} = \frac{\sum_n d_{n,IB} < 0}{\sum_n |d_{n,IB}|} \tag{14}$$

When the immersed body moves, the Eulerian cell velocities inside the body should have the same velocity as the body. This is ensured using equation (15).

$$\bar{U}_{IB} = \frac{d\bar{x}}{dt} + \omega_{IB} \times (\bar{x}_c - \bar{x}_{IB,cm}) \tag{15}$$

where $\bar{x}$ is the direction vector, $\bar{x}_c$ is the cell centre, $\bar{x}_{IB,cm}$ is the mass centroid of the immersed body and ω_{IB} is the angular velocity of the body, which in this case is zero ($\omega IB = 0$) as no rotational motion of the needle is considered.

In the present study, the motion of the needle in three dimensions is pre-defined and its profile is shown in Figure 1. The data file with the time series is interpolated by the immersed boundary model to extract the location of the needle at any time instant.

Two component, cavitating model (liquid, vapour, air)

As described in the previous section, the two-component cavitation model used in this study was

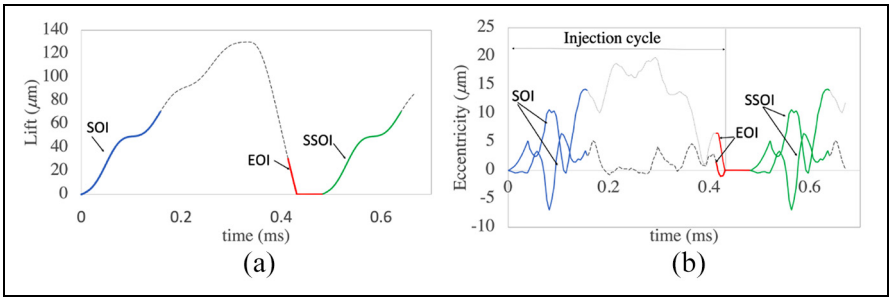

Figure 1. (a) Needle lift profile and (b) eccentricity in x (dashed) and y (dotted) direction as reported in Gold et al.[5] Start of Injection (solid blue), End of Injection (solid red) and Subsequent Start of Injection (solid green).

Table 1. Properties of diesel, vapour and NCG at 60 *bars* and 60°*C*.

	Liquid properties			Vapour properties			Gas properties	
B	0.19	GPa	C_{vap}	1,7036	pa/(kg/m^3)^n	C_{gas}	7,5267.8	pa/(kg/m^3)$^\gamma$
N	7.15	–	κ	1.022	–	γ	1.4	–
ρ_l	880.7	kg/m^3	ρ_v	0.143	kg/m^3			
c_l	1253	m/s	c_v	129.1	m/s			
$P_{sat,L}$	54.9	kPa	$P_{sat,V}$	2336	Pa			
μ_L	4.64	mPa s	μ_V	7.0	μPa s	μ_g	17.8	μPa s

validated and reported by the authors in their previous work.[51] However, for the sake of completeness of this study, the final equation used is given in equation (16) without aiming to present their derivation, as this can be found in Mithun et al.[51] In this equation, the compressibility of the liquid diesel ($\rho \geqslant \rho l$) is modelled using a modified Tait equation with B and N as the bulk modulus and stiffness of the diesel fuel. The mixture phase ($\rho v \leqslant \rho \leqslant \rho l$) is modelled by integrating the Wallis speed of sound for an isentropic flow process. In this equation, c is the speed of sound. The barotropic equation for the pure vapour ($\rho < \rho v$) and non-condensable gas follow the isentropic gas equation with $Cvap$, κ and $Cgas$, γ as the isentropic constant and heat capacity ratio of vapour and NCG respectively. The constants used in equation (16) are given in Table 1.

$$p = \begin{cases} B\left[\left(\dfrac{\rho}{\rho_l}\right)^N - 1\right] + p_{sat,l} & \rho \geqslant \rho_l \\ \dfrac{c_v^2 c_l^2 \rho_l \rho_v (\rho_v - \rho_l)}{c_v^2 \rho_v^2 - c_l^2 \rho_l^2} ln\left(\dfrac{\rho}{c_l^2 \rho_l (\rho_l - \rho) + c_v^2 \rho_v (\rho - \rho_v)}\right) + p_{ref} & \rho_v \leqslant \rho \leqslant \rho_l \\ C_{vap}\rho & \rho < \rho_v \\ C_{gas}\rho & (NCG) \end{cases} \quad (16)$$

Limitations, link to previous works and present contribution

As already mentioned, the present work builds upon earlier and on-going studies published by the authors on simulation of nozzle flows and sprays. To the best of authors knowledge, this is the first study to simulate wall-wetting phenomena in diesel injector nozzles occurring during the opening, closing and dwelt time of the needle valve. More specifically, these are linked one hand with the wave dynamics developing during the closing of the needle valve that induces air entrainment inside the nozzle promoting fuel dribbling, while on the other hand, its eccentric motion further contributes to the development of swirling flow that promotes splashing of the low velocity fuel dribbling from the injector, onto the surfaces of the nozzle.

Before proceeding to the presentation of the results, the limitations arising from both the validity of the models utilised and the selection of the specific conditions investigated, are summarised and evaluated. More specifically, these include: (1) the lack of detailed quantitative validation against experimental data; (2) the assumption of local mechanical and thermal equilibrium under the framework of the homogeneous equilibrium model adopted and (3) the omission of the dependency of fuel properties on pressure and temperature.

(1) With regards to the lack of quantitative experimental validation for the conditions tested, several comments and reference to prior works can be made. Predictions obtained in an enlarged single-hole nozzle utilising a similar barotropic model[58] as the one used here, have been compared against the 3D distribution of cavitation vapour volume fraction derived using X-ray micro computed tomography X-ray; ±7% deviation between simulations and experiments has been reported, considering the detailed quantification of both numerical and experimental uncertainties. Further validation has been obtained for the flow field distribution, cavitation frequency shedding and turbulent velocities in the same single-hole nozzle against high energy X-ray phase contrast imaging (XPCI) measurements for conditions covering a range of cavitation regimes (incipient, fully developed and vortex/string cavitation).[21,22] Additionally, validation against Laser Doppler Velocimetry (LDV) measurements has been also reported in Koukouvinis et al.[59] with deviations within the experimental error. These comparisons give confidence that the barotropic model is performing relatively well for similar cases as those studied here. With regards to validation of the models for realistic nozzle geometries, past studies exist for VCO nozzles;[2,14,60,61] still focus was placed on sprays using a Lagrangian methodology, which cannot predict fuel dribbling. Currently, the data of the ECN represent the most comprehensive database for fuel sprays; relevant predictions have been recently reported;[60] still, effects occurring upon the needle valve closing and the dwelt time between injections have not been studied, while the flow in the single-nozzle considered is a simplification compared to the complex flow distribution in the VCO nozzle studied here. Finally, the recent work[14,39,60,61] provides qualitative validation of a barotropic model against images obtained inside a transparent real-size sac-type nozzle operating at pressures similar to those tested here; this study provides further confidence that the model can capture the co-existence of cavitation vapour and air entrainment during the closing phase of the needle valve and during the dwelt time. As already mentioned, the present manuscript includes further qualitative comparison of the model predictions against the experimental data reported recently by the authors in Gold et al.[5] and also the work of Manin et al.[53]

(2) One of the main assumptions in the described methodology is the mechanical and thermodynamic equilibrium between the liquid, vapour and air. With regards to the mechanical equilibrium assumption, the recent studies from the authors using a two-fluid model have confirmed that differences between liquid and vapour velocities are less than 10% and only in localised locations of the flow,[62,63] while they do not affect the overall growth rate and production of vapour. With regards to thermodynamic equilibrium assumption, a metastable, that is, non-thermodynamic equilibrium, state occurs when the pressure of the liquid drops below the saturation pressure and no vapour is formed due to the rapid expansion of the liquid.[64,65] In the literature, the well-known Schnerr and Sauer,[66] Singhal et al.[67] and Zwart et al.[68] non-thermodynamic equilibrium (mass transfer rate) models are widely used. Such models can tend towards equilibrium by using large mass transfer terms, that is, increasing the evaporation/condensation coefficients.[21,69] To estimate the time scales of such phenomena relative to the residence time of the fuel through the injector, the relaxation time of the tensile stresses, that is, those acting in the metastable state, has been numerically estimated to be of the order of 10 ns for a vertical tube filled with liquid, impacted vertically, suddenly and producing an expansion wave of 30 MP.[70] The residence time of the fluid in the injection hole is of the order of ~1.5 μs, for an injection pressure of 160 MPa case; thus, the time to reach equilibrium would be, at least, 150 times faster. As a result, predictions obtained using homogeneous mixture models[59,71] exhibit very similar performance to those obtained using large mass transfer rates.

(3) Finally, the present study assumes isothermal flow and adiabatic nozzle walls; thus, it neglects the dependency of fuel properties on pressure and temperature and heat transfer on the nozzle walls. This is justified by the fact that the injection pressure of ~160 MPa utilised in pilot injection events, as those tested here, result to temperature difference of less that ~20°C; see selectively[72–77] for fixed needle lift and transient needle lift studies in Salemi et al.,[78] Strotos et al.[79] At the same time, recent measurements for the diesel fuel properties have been reported and modelled using advanced equations of state, such as the PC-SAFT.[60,80–82] For the pressure range investigated here, it can be estimated that the variation of fuel properties is practically negligible and renders the additional complexity of such approaches out of the scope of the present work. Moreover, the time it takes for the liquid wetting the nozzle walls to heat up and gradually vapourise, is orders of magnitude longer compared to the short time interval simulated here;[42,43] thus, the assumption of adiabatic nozzle wall is justified.

Problem description

The numerical models developed are implemented into Ansys Fluent using user defined functions. The geometry of the six-hole valve covered orifice (VCO) nozzle and the details about the computational domain and numerical grids are shown in Figure 2. The computational domain is extended at the outlet body of the injector in order to model the combustion chamber in

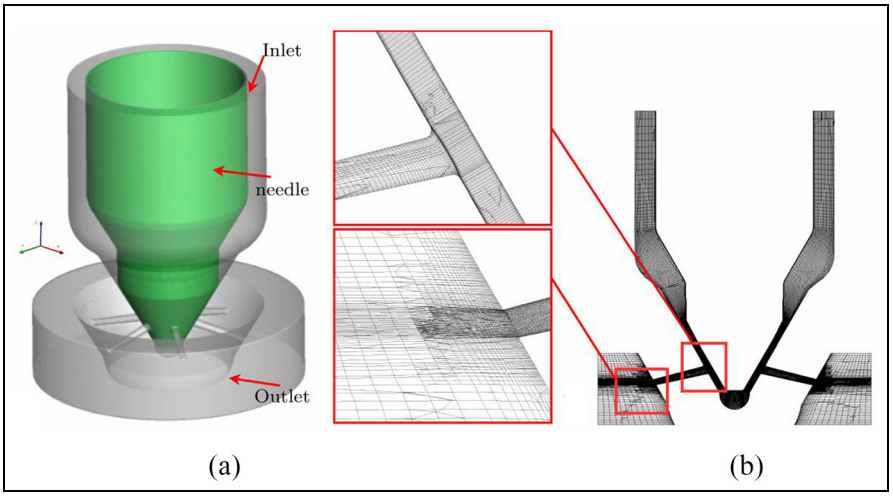

Figure 2. (a) VCO geometry and (b) cross-section of the hexahedral mesh highlighting the mesh details near orifice entrance and exit. Telescopic refinement near the wall to ensure $y^+ \sim 1$.

the vicinity of the nozzle exit; this is initialised with 100% NCG at the beginning of the simulation. The inlet and outlet boundaries are applied with a constant absolute pressure of 1600*bars* and 60*bars*, respectively. The computational domain is discretised using hexahedral elements with telescopic boundary layer refinements near the wall to maintain the y^+ values close to 1 suitable for the $k-\omega-SST$ model. The computational domain is split into two regions: one within the interior of the injector nozzle and the other which is exterior to the injector where the diesel is injected. Since the main focus of this study is to predict the dribble formation and wall surface wetting caused by the dribbles near the orifice exit at needle closure, special attention was given to the mesh resolution near the needle seat and the orifice exit. In particular, a resolution of $0.5\mu m$ is applied near the needle seat and $1.75\mu m$ near the orifice walls. In addition to that, the mesh near the exit is refined using a non-conformal mesh as shown in the subset of Figure 2(b). The resolution at the core of the orifice is in the range of $5\mu m$. The same resolution is used in the near nozzle region which allows liquid fragments larger than $5\mu m$ to be simulated. To minimise the computational cost, the nozzle downstream is meshed with larger aspect ratio elements which could influence the shape of the droplets. With these refinements, the total mesh count is approximately 10 million cells with ~6 million inside the injector and ~4 million cells outside of the injector. On the other hand, the resolution for the temporal discretisation is chosen such that the convective Courant number is in the range of unity (CFL ~ 1). The physical properties of the diesel used are given in Table 1.

Validation of the model

One of the biggest challenges in validating the numerical models such as the one presented in this work is the absence of more rigorous physical validation measurements. In the absence of such quantitative data, qualitative comparisons such as flow structures, ligaments, etc., is a good and interesting first approach. In Figure 3, the flow structures predicted by the current numerical model shows a good match with the experimental observations. In addition to that, the applicability of the numerical model with moving geometry is further validated against the experimental data obtained for a single hole nozzle;[53] these correspond to a modified single-hole transparent nozzles manufactured with the same hole inlet radius and diameter as in Engine Combustion Network (ECN) Spray D nozzle, while the body and needle geometry correspond to that of the ECN Spray A nozzle; this is shown in Figure 4. The nozzle is imposed with an upstream pressure of 500*bar* and a downstream pressure of 1 bar. The needle motion profile used by the authors of Manin et al.[53] is shown in Figure 4(b). To replicate the experimental conditions, the model is initialised with diesel fuel inside the nozzle and ambient gas inside the circular chamber.

The qualitative validation of the events during the start and end of injection shown in Figure 5. Figure 6 is in good match with the experimental results. The numerical model predicts the retraction of the liquid and the formation of the leading-edge umbrella during the start of injection (Figure 5), and the bulk cavitation and gas pull back during end of injection (Figure 6) as observed in the experiment.

Results and discussion

In this section, the results obtained are presented for the two phases considered during the operation of the injector nozzle. The dynamics of the flow inside the orifices and the development of the spray during the start of injection from a fully filled with liquid nozzle is presented first. The flow during the end of injection and after the needle closure (dwelt time period), which shows the near-nozzle fuel dribbles is presented next, followed by the simulation of the subsequent start of injection.

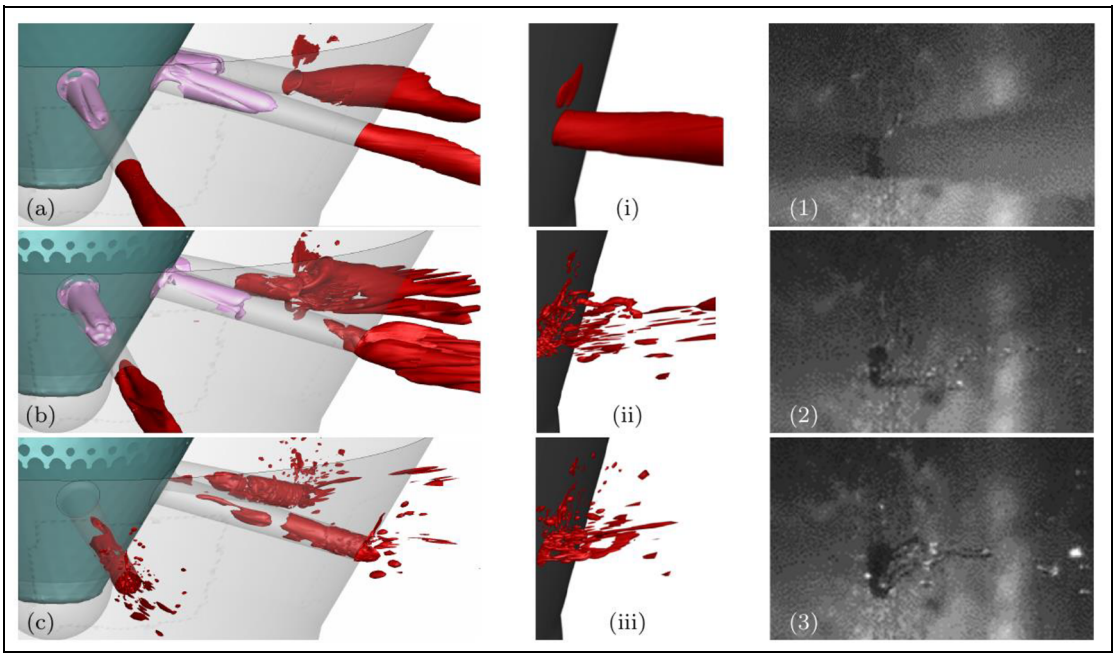

Figure 3. Validation of the numerical model showing the liquid jet break-up during end of injection. (a–c) and (i–iii) are the results from current simulation matching the experimental visualisation, (1–3) are the experimental results from Gold et al.[5] at 800 μs ASOI, 1000 μs ASOI and 1100s ASOI. Isosurface of 90% gas volume fraction (red) and 50% vapour volume fraction (pink) is shown.

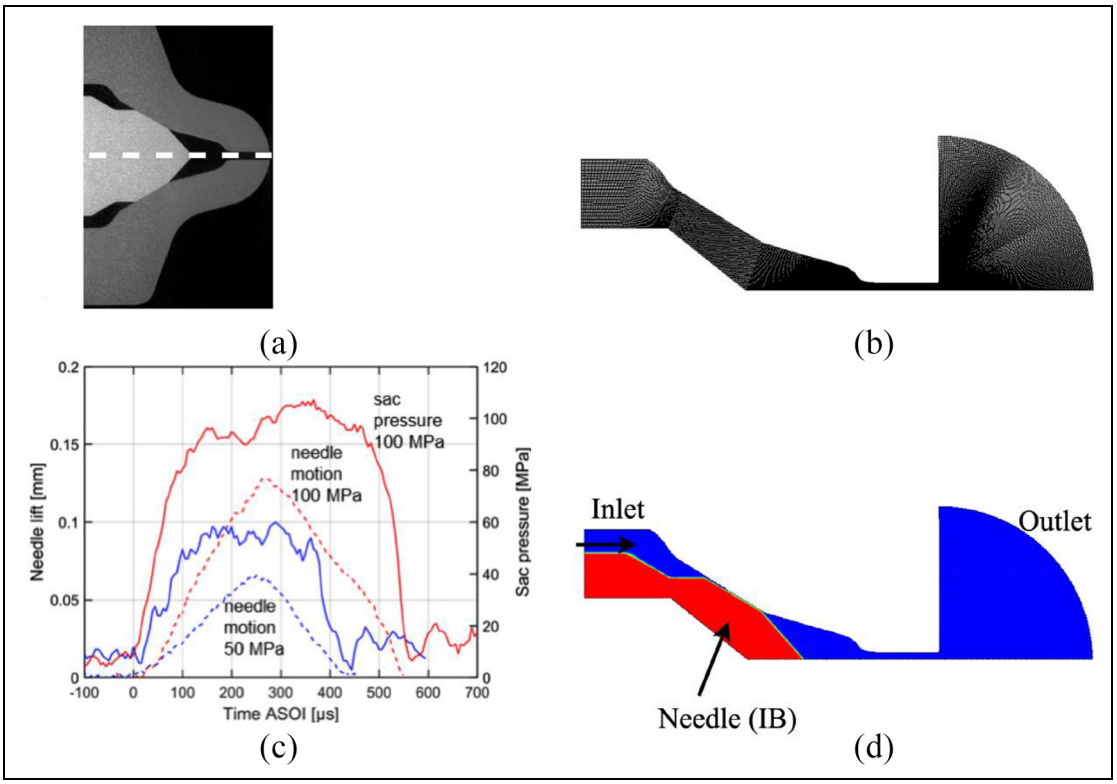

Figure 4. (a) Single hole ECN Spray D nozzle. (b) Needle motion profile as obtained from Manin et al.[53] for different injection pressure. (c) The hexahedral numerical mesh showing the extended circular chamber. (d) IBM representation of the needle (in red).

Start of injection transients

In this section, the flow development inside and outside the nozzle orifice during the start of injection is presented. During the start of injection, the nozzle orifice is assumed to be filled with diesel and the gas is present only in the engine chamber. The needle rests on

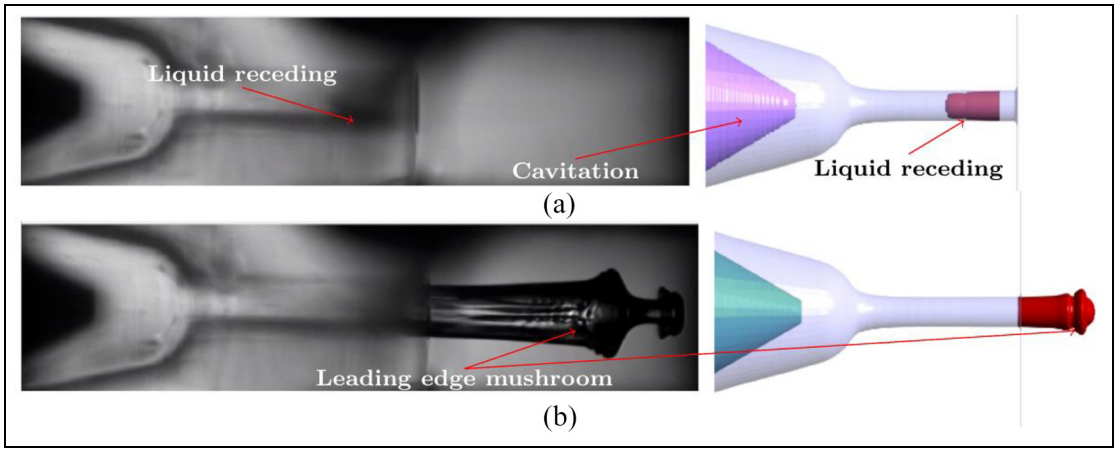

Figure 5. Validation of the numerical model with the experimental results from Manin et al.[53] during the start of injection event.

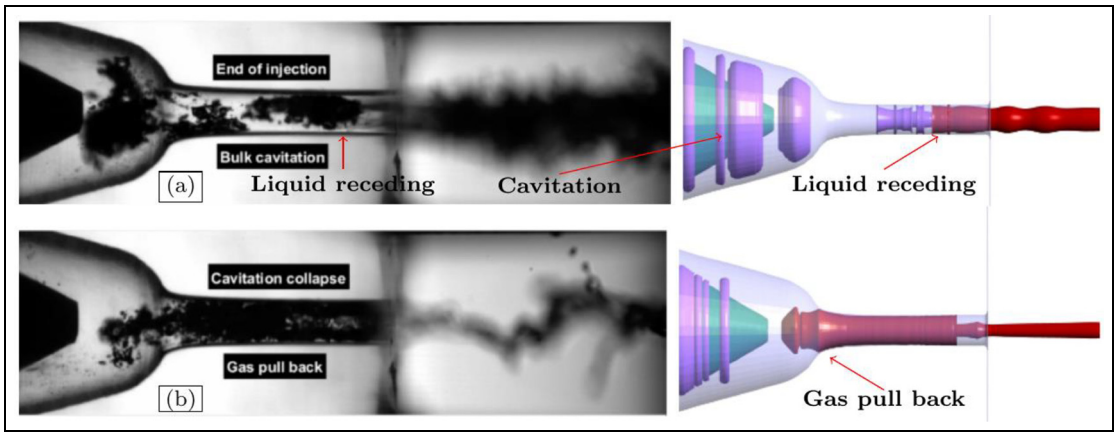

Figure 6. Validation of the numerical model with the experimental results from Manin et al.[53] during the end of injection event.

its seat sealing the flow between the inlet and outlet. The Start of injection transients (SOI) simulation is performed for a needle lift up to $70\mu m$ starting from a fully closed condition as depicted in Figure 1 following the solid blue line.

When the needle lifts from its closed position, the suction created due to the sudden acceleration of the needle pulls in a small amount of air from the combustion chamber into the orifice (Figure 7(a)), forming a concave liquid front inside the orifice. The sudden opening of the needle also produces local counter-rotating vortices just below the needle valve, resulting in the formation of cavitation bubbles at this location, also shown in Figure 7(a). With the further lifting of the needle valve, the fuel slowly recedes into the orifice. The backward flow of the air stops and the forward motion of the fuel towards the orifice exit starts when the needle lift reaches approximately $5\mu m$ for this specific nozzle design. At this low lift, the high pressure at the inlet produces highly accelerated flow in the gap between the needle and nozzle walls, which is sufficient to generate cavitation at the inlet edge (see Figure 7(b) at $10\mu m$). At the same time, the formation of a mushroom-headed jet can also be seen outside the orifices (Figure 7(b)). The penetration of the liquid jet into the combustion chamber and the formation of cavitation occurring in each orifice correspond to different rates, due to the hole-to-hole flow variations caused by the eccentric needle motion. Further lifting of the needle valve induces a highly swirling flow inside the orifice holes and result in the formation of vortex cavitation in addition to geometry-induced cavitation[83,84] realised at the hole inlet, as can be seen from Figure 7(c) onwards. Both the vorticity-induced and geometry-induced cavitation stretch and merge along the orifice axis resulting in the formation of string cavities as the needle lifts further (Figures 7(d) and 8(b)). Two types of string cavities are particularly noted, one that originates from the orifice inlet towards the outlet and the other which starts from the air downstream towards the upstream direction, as highlighted in Figure 7(d) and (f); a similar formation of string cavitation from an enlarged VCO was also observed by Gavaises et al.[85] in their experimental study. The two string cavities from both ends stretch towards each other and merge to form a single long string cavity starting from the needle towards the

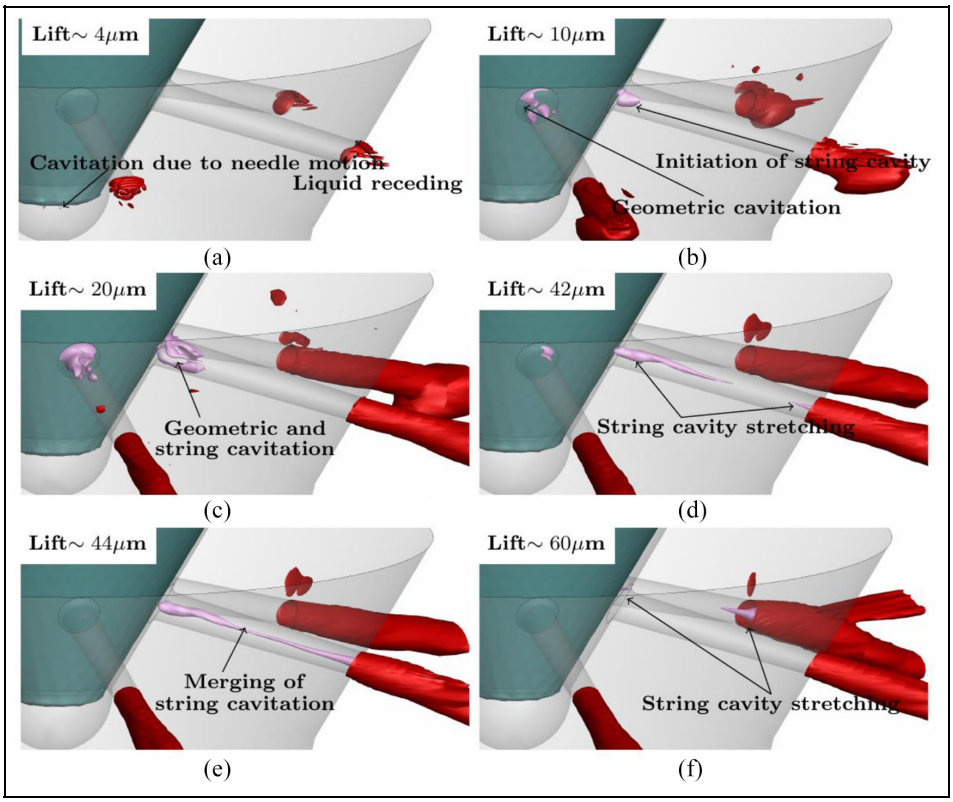

Figure 7. Evolution of diesel jet and formation of cavitation during start of injection showing the development of geometry-induced cavitation and the stretching of string cavitation during the needle opening is shown at selected needle lifts (a–f). Isosurfaces of 90% gas volume fraction (red) and 50% vapour volume fraction (pink) is shown.

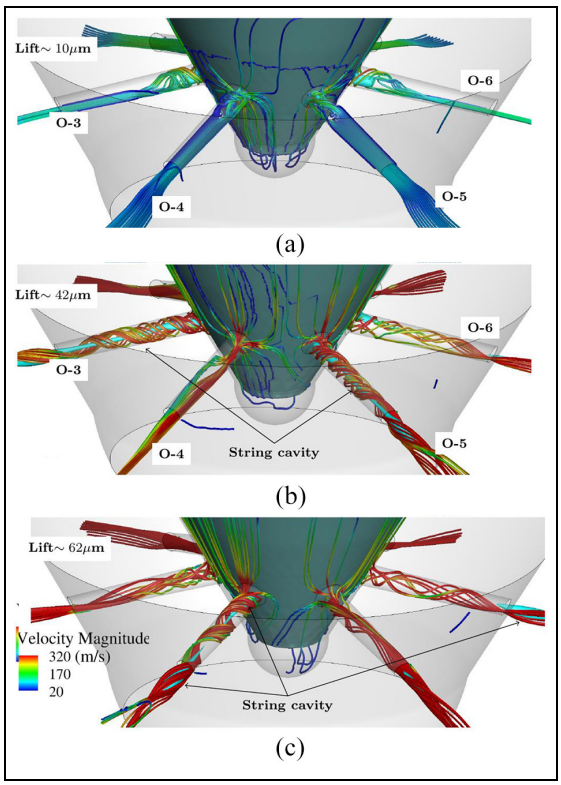

Figure 8. Detailed view of swirling flow and string cavitation at selected needle lifts during SOI (a–c). Streamlines coloured with velocity magnitude and the isosurface of 50% vapour volume fraction shown in cyan.

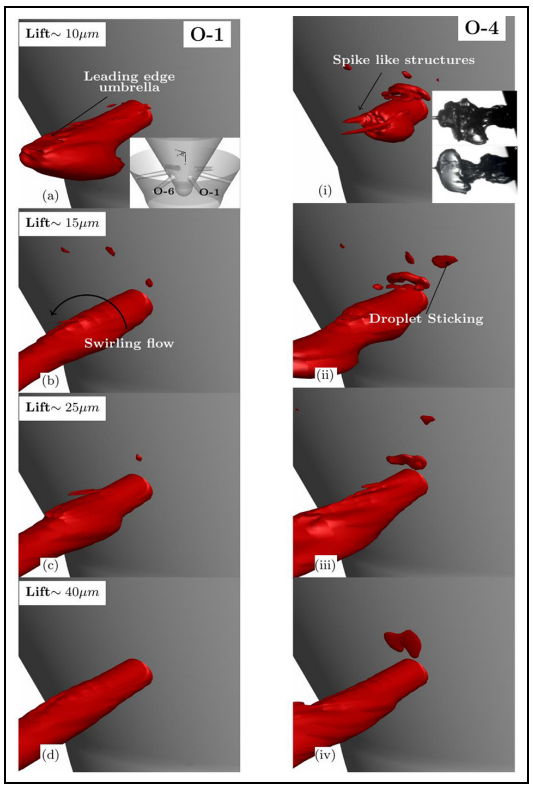

Figure 9. Dribble formation during start of injection from a nozzle filled with diesel. Correlation with the experimental observation from Gold et al.[5] shown in the subset of (i). Isosurface of 90% gas volume fraction is shown in red. Figures are shown selectively for (a–d) Orifice 1 and (i–iv) Orifice 4.

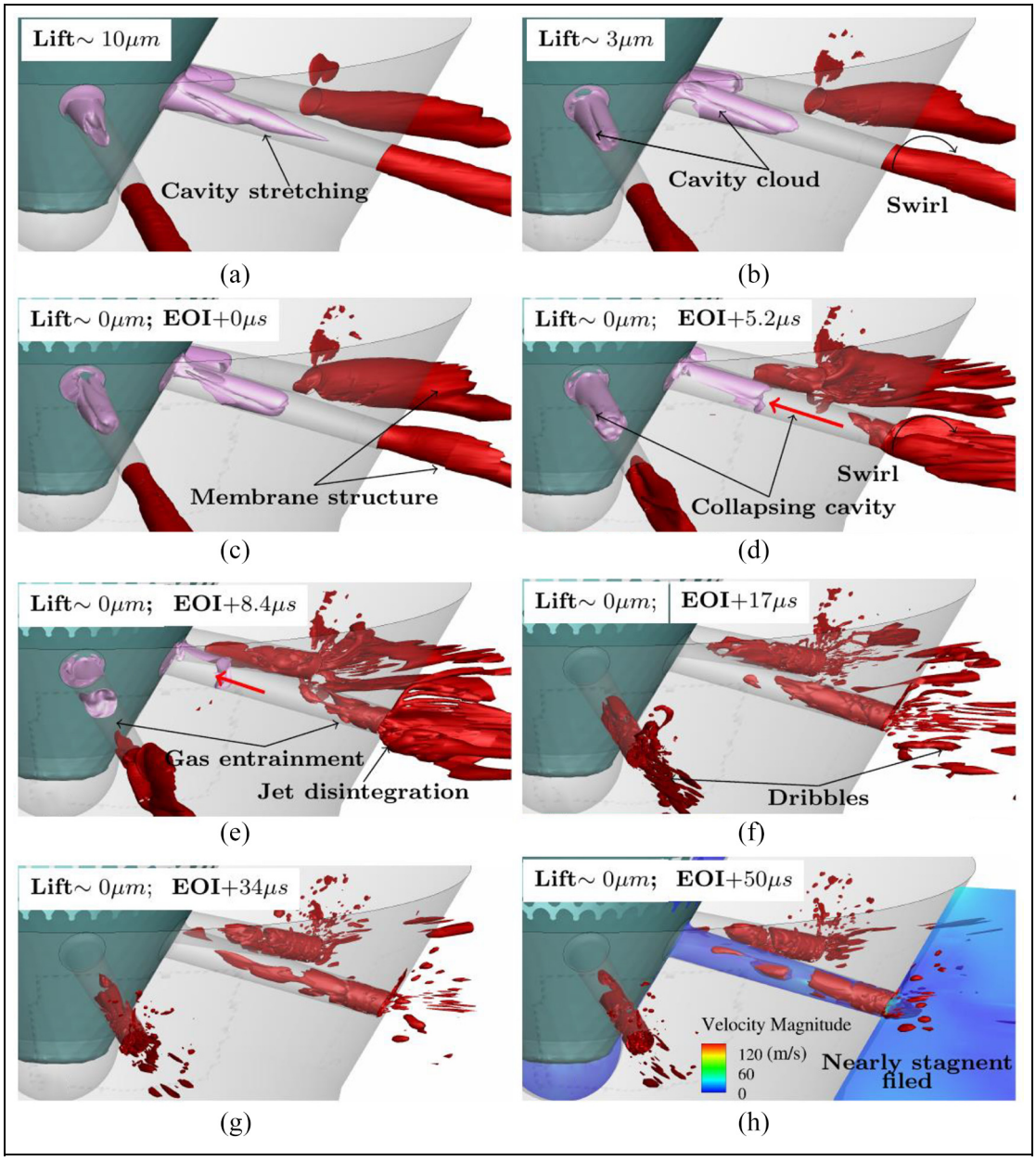

Figure 10. Break-up of diesel jet and cavitation formation inside the orifice during end of injection. The sequence (a–h) shows the cloud cavity stretching and the entrainment of gas after the needle closure. Isosurface of 90% gas volume fraction (red) and 50% vapour volume fraction (pink) is shown.

combustion chamber, as shown in Figure 7(e). A more detailed view along with the streamlines showing the swirling flow and the formation of string cavitation at the core of this vortices is shown in Figure 8. These string cavities are dynamic in nature and are observed in pairs simultaneously from orifices O-3, O-5 and O-4, O-6 at different needle lifts, starting from $\sim 40\mu m$. Two such instances showing the development of string cavities from orifice pairs are given in Figure 8(b) and (c). The simulation of SOI is terminated at $\sim 70\mu m$ needle lift where the cavitation does not appear inside the nozzle any further and no large-scale oscillations appear on the diesel jet.

Focusing on the flow outside of the nozzle, when the needle lifts-off from its seat, the high injection pressure at the inlet forces the diesel fuel to flow out of the orifice into the combustion chamber. As the flow progresses, the diesel jet forms a leading-edge umbrella with surface instabilities in the form of spike-like structures emanating from the head of the umbrella, as it can be seen from Figure 9(i). The downward inclination of the orifices (see the subset of Figure 9(a)) induces higher acceleration at the upper half of the orifice compared to the lower half, causing an umbrella front to be stretched more in the upper half. As the needle valve lifts further, allowing more flow into the nozzle, the diesel jet penetrates into the chamber against the air, forming large ligaments and droplets from its periphery. The initial droplets formed are larger in size and non-spherical in shape. It is observed that some of

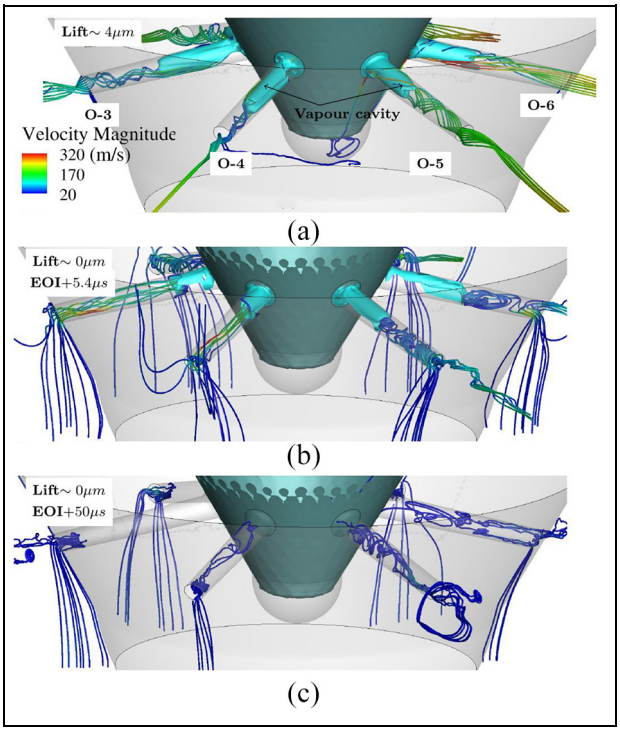

Figure 11. Detailed view of swirling flow and string cavitation at selected needle lifts (a–c) during EOI. Streamlines coloured with velocity magnitude and the isosurface of 50% vapour volume fraction shown in cyan.

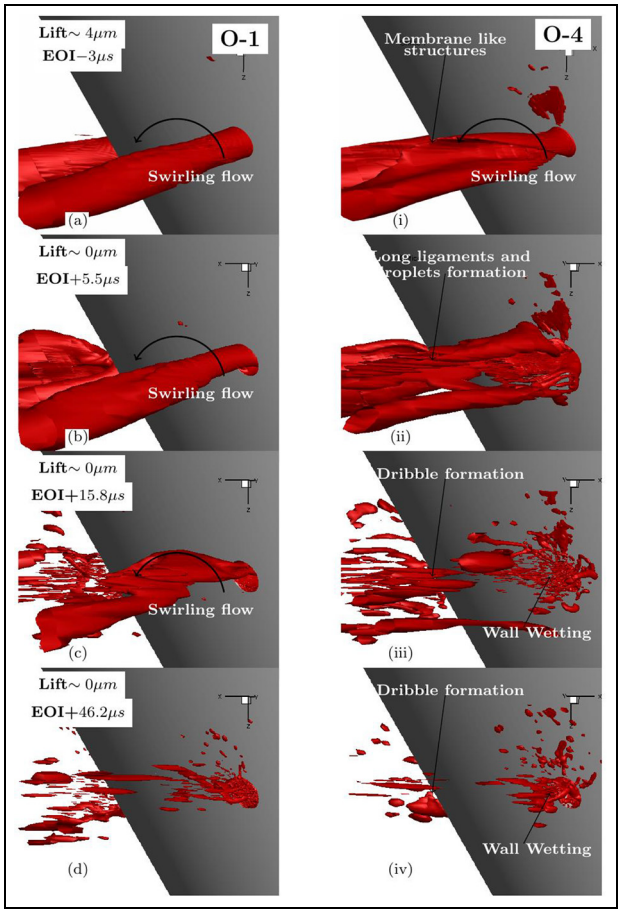

Figure 12. Isosurface of 90% gas volume fraction showing the disintegration of diesel jet during and after the needle closure. The swirling motion creating a membrane like structure and the formation of large ligaments and droplets later causing wall wetting is also shown. Figures are shown selectively from (a–d) Orifice 1 and (i–iv) Orifice 4.

these initial droplets formed lose their momentum and tend to stick to the nozzle wall, due to wall adhesion, as shown throughout in Figure 9. When the slow-moving liquid droplets come in contact with the oleophilic surface of the nozzle, the surface tension causes them to contract and leave them in the near nozzle region leading to surface wetting. Sticking of these droplets to the wall is observed near all six orifice exits. However, the number of droplets sticking, and the duration of their existence are different for each orifice, due to hole-to-hole variations in the flow. These droplets remain as a residual fuel from the injection and act as a locally rich mixture near the wall.

End of injection transients

The red solid lines in the profile shown in Figure 1 represents the region for which the end of injection simulation is performed. The downward motion of the needle is performed until its complete closure; the simulation further is continued for $50\mu s$ at the closed condition in order to capture the phenomena occurring after the needle closure. The dynamics of flow during the EOI is shown in Figures 10–12 using iso-surfaces of vapour volume fraction and the NCG inside and outside of reaching in the range of $\sim 1000pa(abs)$; this is much lower than the vapour pressure of the diesel fuel considered, thus forming localised cavitation zones near the orifice inlet; see Figure 10(a) and (b). Unlike the narrow string cavitation formed during the SOI, the cavitation formed during the EOI is a more pronounced cavity cloud that covers almost the entire cross-section of the orifice, as can be seen from Figure 10(a) and (b). The eccentric motion of the needle becomes more evident below this needle lift. With the needle valve covering some of the orifices more compared to the other due to its eccentric motion, the disintegration of the liquid jet from these orifices occurs earlier than from those which are less covered by the valve; this is evident while comparing the spray formation from orifices O-1 and O-4 in Figure 12. Even when the flow is completely cut-off by the needle closure (EOI + $0\mu s$), the liquid inside the orifices continue to flow outwards but slowed down from the pressure of the surroundings. Once the liquid bulk has lost its momentum, the back-pressure from the combustion chamber pushes the ruptured liquid inside the orifices back towards the inlet, recovering the pressure inside and collapsing the vapour cavities, as it can be observed from Figure 10(d) onwards. Behind the ruptured residual liquid, large pockets of gas from the chamber also enters the orifices. The receding of the diesel, as well as the entrainment of gas into the orifice,

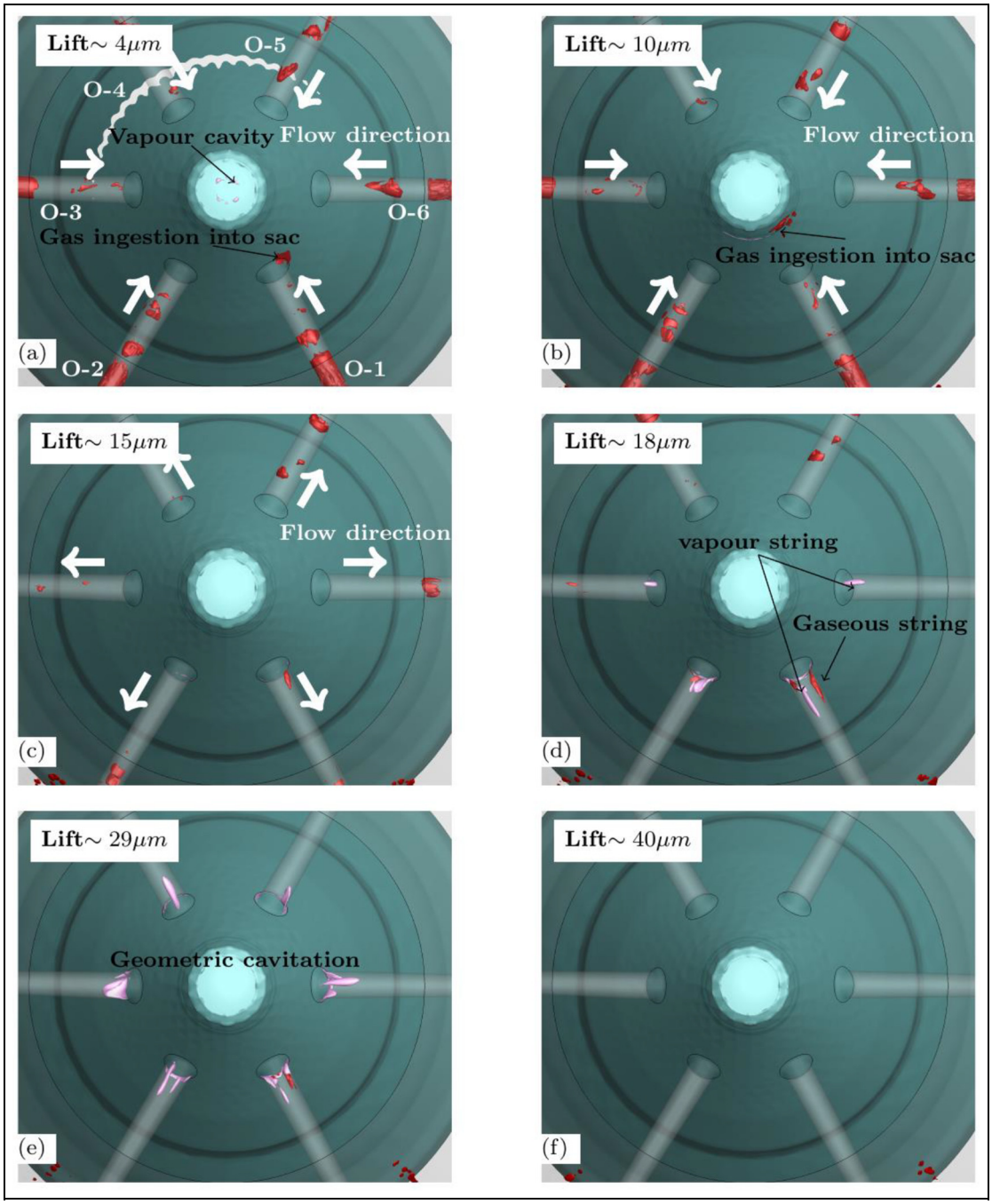

Figure 13. Evolution of diesel jet and formation of cavitation during subsequent start of injection shown using a view from the bottom of the injector (a–f). The presence gas bubbles inside the orifices and the ingestion of gas into the sac volume is depicted using iso-surface of 90% gas volume fraction (red) and 50% vapour volume fraction (pink).

is seen until the vapour cavity present in the orifice is completely collapsed, after which the entrained gas is found to oscillate due to the fluctuating pressure field. Such a pressure field oscillation after the end of injection was also reported by Manin et al.[53] on a single hole nozzle injector with supporting evidence in the form of slow-motion videos. The complete collapse of vapour cavities from the nozzle occurs about $17\mu s$ after the EOI in this particular nozzle; by then 50% of the orifice length is filled with the gas from the combustion chamber. After $\sim 34\mu s$, the velocity field becomes almost stagnant with only negligible flow oscillations inside the orifices and relatively small movement of droplets observed outside the orifices. The EOI simulation is stopped at $\sim 50\mu s$ after the needle closure when the flow became stagnant everywhere in the computational domain; this can be seen from the contour of the velocity magnitude shown at a mid-plane of the orifice in Figure 10(h). The compressible gas inside the orifices influences the subsequent injection process. The presence of gas voids inside the orifice prior to the start of injection was also observed by Mitroglou et al.[24] in

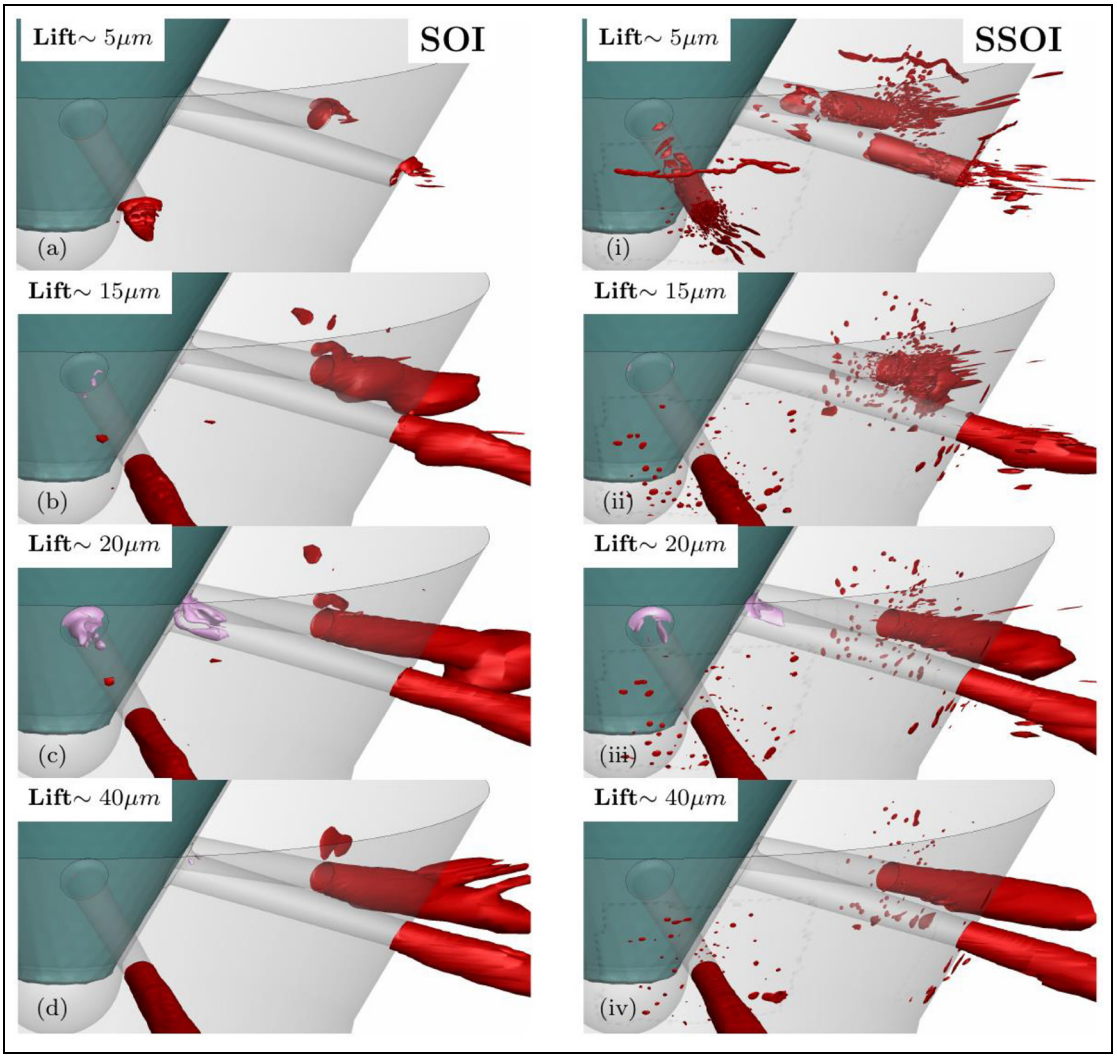

Figure 14. Comparison between (a–d) SOI and (i–iv) SSOI at different needle lift showing the delay in jet formation due to the presence of entrained gas in the orifice. Iso-surfaces of 90% gas volume fraction shown in red and 50% vapour volume fraction shown in pink.

their experimental visualisation from a real-size, multi-hole, transparent, sac-type injector. They reported that the bubble patterns observed are not repeatable and they can be found either as a single large or as multiple smaller bubbles. Given sufficient time, with repeated injection cycles, these bubbles can coalesce and form a large void that can occupy most of the sac volume.

Subsequent start of injection

The subsequent injection after the end of the previous injection cycle starts from a completely closed needle position where the liquid droplets are shown with the solid green lines in Figure 1. At the SSOI, the orifice is partially filled with gas from the previous injection. The eccentricity in needle motion causing the orifices in the upper half being partially covered is evident from Figure 13(a). The formation of cavitation under the needle valve created due to vortices generated during the sudden opening of the valve can also be seen in Figure 13(a). As the needle lifts-off from its seat, the suction created by the needle motion pulls some gas that is already present inside the orifice further towards the needle valve and also into the sac volume. By comparing the instances shown in Figure 13(a) and (b), the ingestion of the gas into the sac can be traced. The presence of gas inside the sac volume during the start of injection was also observed by Swantek et al.,[4] Mitroglou et al.[24] in their experimental studies. The suction of the gas into the sac continues until about $11\mu m$ needle lift, after which the gap between the needle valve and the sac wall is sufficient to induce forward flow from each orifice pushing the gas back into the chamber, an instance is shown in Figure 13(c) at $15\mu m$ needle lift. With the further lifting of the needle valve, the forward flow is established and the formation of a cavitating vortex from the orifice inlet can be observed. In addition to the cavitating string, during SSOI a string of expanding gas from the orifice inlet coexist with the vapour string, as it can be seen from Figure 13(d). Unlike the string cavities that extend towards the orifice exit as observed during SOI, the formation of the vapour and gaseous strings during

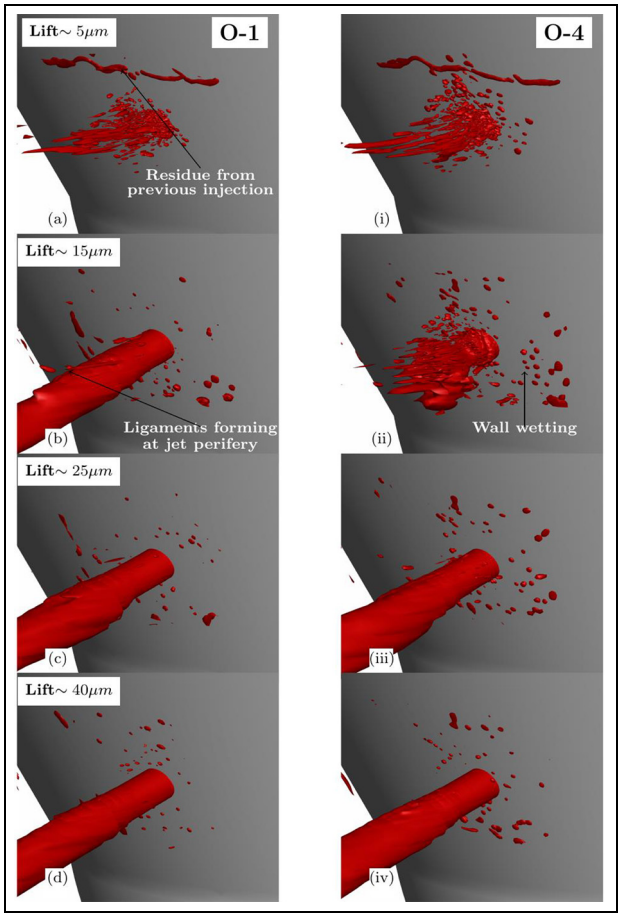

Figure 15. Isosurface of 90% gas volume fraction showing the residual droplets and the newly formed droplets sticking to the wall due to adhesion during subsequent start of injection. Figures are shown selectively from (a–d) Orifice 1 and (i–iv) Orifice 4.

SSOI does not seem to stretch more than ~30% of the orifice length. In addition to that, the formation of string cavity that originated from the combustion chamber towards the orifice inlet during SOI is also not observed during SSOI. The cavitation inside the orifices disappears completely when the needle lift is about $40\mu m$ for this particular design, which is much earlier compared to the SOI. This could be attributed to the recovery of local pressure due to expansion of the gas present inside the orifice when the pressure drops, thus limiting the cavitation formation at the orifice inlet compared to SOI and EOI. A comparison of flow field between SOI and SSOI at different needle lifts is given in Figure 14. It can be confirmed from this figure that the presence of the compressible gas inside the orifice delays the penetration of the diesel jet from the nozzle and limits cavitation. However, due to earlier disappearance of cavitation, the fluctuations in the periphery of the diesel jet also disappear earlier during SSOI compared to SOI where cavitation exists for a longer period.

On the nozzle wall surface, which is in contact with the combustion chamber, the number of droplets sticking is much higher compared to that seen during SOI situation. This is primarily due to the residue from the previous injection being present inside and near the orifice exit. As the needle lifts-off from its seat, the swirling flow forces more droplets onto the wall as liquid dribbles and agglomerates, forming larger droplets and ligaments; this can be seen in Figure 15(a, i) along with the formation of the spike-like structure at the periphery of the diesel jet. A delay in the formation of diesel jet can also be observed while comparing the orifices O-1 and O-4 in Figure 15(b, ii) which is influenced both by the eccentricity as well as the entrained gas. With the further lifting of the needle valve, the flow from all orifices becomes established and the droplets and ligaments formed at its periphery continue to stick to the wall as before causing wall-wetting. The diesel jet becomes fully established above $\sim 45\mu m$. With the lifting of the needle, the number of droplets sticking to the wall also decreases. It is noted that the size and number of droplets present on and near the wall during SSOI are much larger compared to the SOI at all needle lifts. The simulation was terminated after the needle reaching a lift of $\sim 60\mu m$. It is expected that over multiple injection cycles, some of these droplets sticking on the wall may either merge and form large droplets before escaping from the wall or may evaporate from the wall at higher temperatures present inside the chamber.

Conclusion

Fuel dribbling and external nozzle wall wetting occurring during the opening, closing, dwelt time of the needle valve of a diesel injector nozzle have been simulated numerically by solving the Navier-Stokes equations, utilising a fully compressible two-phase two-component barotropic model; the barotropic fluid was assumed to be in thermal and mechanical equilibrium with the air, while an additional transport equation coupled with the VOF interface capturing method has been utilised to resolve the liquid-gas interface. The six-hole VCO injector nozzle has been simulated imposing realistic conditions of the valve movement and considering in addition to its axial motion, a time-dependent eccentric motion. The valve motion has been simulated utilising the immersed boundary method; that has allowed for predictions to be obtained at zero valve lift during the dwelt time between successive injections, where the needle remains closed. The model predicted the formation of vortex (or so-called string) cavities stretching from the needle surface till the orifice exit, along with the formation of small droplets and ligaments at the near nozzle exit region. The eccentric needle motion was found to be responsible for the formation of strong swirling flows inside the orifices, which not only contributes to the breakup of the injected liquid jet into ligaments but also to their backwards motion towards the external wall surface of the injector. After their splash, the liquid fragments have been found to splash and stick to the nozzle walls. Model predictions have been qualitative

compared against images of the near-nozzle spray as well as cavitation and air entrainment obtained in both the VCO six-hole nozzle and the ECN single hole injector and found in reasonably good agreement. It is found that wall wetting phenomena are more pronounced during the closing period of the valve and fuel injection in subsequent injection events, due to the residual gases trapped inside the nozzle, which contribute to the pure atomisation of the injected fluid.

Declaration of conflicting interests

The author(s) declared no potential conflicts of interest with respect to the research, authorship, and/or publication of this article.

Funding

The author(s) received no financial support for the research, authorship, and/or publication of this article.

ORCID iD

Mithun Murali-Girija https://orcid.org/0000-0002-7118-8413

References

1. Heywood J. *Internal combustion engine fundamentals*. New York, NY: McGraw-Hill, 1988.
2. Gavaises M. Flow in valve covered orifice nozzles with cylindrical and tapered holes and link to cavitation erosion and engine exhaust emissions. *Int J Engine Res* 2008; 9: 435–447.
3. Reitz RD, Ogawa H, Payri R, et al. IJER editorial: the future of the internal combustion engine. *Int J Engine Res* 2020; 21: 3–10.
4. Swantek AB, Duke D, Tilocco FZ, et al. End of injection, mass expulsion behaviors in single hole diesel fuel injectors. In: *Proceedings of international liquid atomisation and spray systems conference (ILASS Americas)*, Portland, OR, 2014.
5. Gold M, Pearson R, Turner J, et al. Simulation and measurement of transient fluid phenomena within diesel injection. *SAE Int J Adv Curr Pract Mobility* 2019; 1: 291–305.
6. Pierpont DA and Reitz RD. Effects of injection pressure and nozzle geometry on D.I. diesel emissions and performance. SAE paper 1995-950604. 1995.
7. Sayin C, Uslu K and Canakci M. Influence of injection timing on the exhaust emissions of a dual-fuel CI engine. *Renewable Energy* 2008; 33: 1314–1323.
8. Pierpont DA, Montgomery DT and Reitz RD. Reducing particulate and NOx using multiple injections and EGR in a D.I. diesel. SAE technical paper 950217, 1995.
9. Dürnholz M, Endres H and Frisse P. Preinjection a measure to optimize the emission behavior of DI-diesel engine. SAE paper 940674, 1994.
10. Molina S, Salvador FJ, Carreres M, et al. A computational investigation on the influence of the use of elliptical orifices on the inner nozzle flow and cavitation development in diesel injector nozzles. *Energy Convers Manage* 2014; 79: 114–127.
11. Mithun M-G, Koukouvinis P and Gavaises M. Numerical simulation of cavitation and atomization using a fully compressible three-phase model. *Phys Rev Fluids* 2018; 3: 064304.
12. Giannadakis E, Papoulias D, Theodorakakos A, et al. Simulation of cavitation in outward-opening piezo-type pintle injector nozzles. *Proc Inst Mech Eng Part D J Automob Eng* 2008; 222: 1895–1910.
13. Koukouvinis P, Gavaises M, Li J, et al. Large Eddy Simulation of Diesel injector including cavitation effects and correlation to erosion damage. *Fuel* 2016; 175: 26–39.
14. Gavaises M, Papoulias D, Giannadakis E, et al. Comparison of cavitation formation and development in Diesel VCO nozzles with cylindrical and converging tapered holes. In: *Thermo- and fluid-dynamic processes in diesel engines (THIESEL 2008)*, Valencia, 2008.
15. Battistoni M, Xue Q, Som S, et al. Effect of off-axis needle motion on internal nozzle and near exit flow in a multi-hole diesel injector. *SAE Int J Fuels Lubr* 2014; 7: 167–182.
16. Örley F, Hickel S, Schmidt SJ, et al. LES of cavitating flow inside a diesel injector including dynamic needle movement. *J Phys Conf Ser* 2015; 656: 012097.
17. Arcoumanis C, Gavaises M, Argueyrolles B, et al. Modeling of pressure-swirl atomizers for GDI engines. SAE technical papers 1999-01-0500, 1999.
18. Huang W, Moon S, Gao Y, et al. Hole number effect on spray dynamics of multi-hole diesel nozzles: an observation from three- to nine-hole nozzles. *Exp Therm Fluid Sci* 2019; 102: 387–396.
19. Huang W, Moon S, Gao Y, et al. Eccentric needle motion effect on near-nozzle dynamics of diesel spray. *Fuel* 2017; 206: 409–419.
20. Moon S, Huang W and Wang J. First observation and characterization of vortex flow in steel micronozzles for high-pressure diesel injection. *Exp Therm Fluid Sci* 2019; 105: 342–348.
21. Karathanassis IK, Koukouvinis P, Kontolatis E, et al. High-speed visualization of vortical cavitation using synchrotron radiation. *J Fluid Mech* 2018; 838: 148–164.
22. Karathanassis IK, Trickett K, Koukouvinis P, et al. Illustrating the effect of viscoelastic additives on cavitation and turbulence with X-ray imaging. *Sci Rep* 2018; 8: 14968.
23. Mitroglou N, Gavaises M, Nouri JM, et al. Cavitation inside enlarged and real-size fully transparent injector nozzles and its effect on near nozzle spray formation. In: Cossali GE and Tonini S (eds.) *Proceedings of the DIPSI workshop 2011. Droplet impact phenomena & spray investigations*, 2011, pp. 33–45. Bergamo, Italy: Dipartimento di Ingegneria industriale, Università degli studi di Bergamo.
24. Mitroglou N, McLorn M, Gavaises M, et al. Instantaneous and ensemble average cavitation structures in diesel micro-channel flow orifices. *Fuel* 2014; 116: 736–742.
25. Liu F, Li Z, Wang Z, et al. Dynamics of the in sac cavitating flow for diesel spray with split injection strategy. *Int J Engine Res*. Epub ahead of print 3 September 2020. DOI: 10.1177/1468087420951330.
26. Papadopoulos N and Aleiferis P. Numerical modelling of the in-nozzle flow of a diesel injector with moving needle during and after the end of a full injection event. *SAE Int J Engines* 2015; 8: 2285–2302.

27. Kook S, Pickett LM, Musculus MPB, et al. Liquid-phase diesel spray penetration during end-of-injection transient. In: *Proceedings of the 7th International Conference Model Diagnostics Advanced Engine Systems. COMODIA 2008*, Sapporo, Japan, 2008, pp. 413–420.
28. Kook S, Pickett LM and Musculus MPB. Influence of diesel injection parameters on end-of-injection liquid length recession. *SAE Int J Engines* 2009; 2: 1194–1210.
29. Musculus MPB. Entrainment waves in decelerating transient turbulent jets. *J Fluid Mech 2009*; 638: 117–140.
30. Eagle WE and Musculus MPB. Cinema – stereo imaging of fuel dribble after the end of injection in an optical heavy – duty diesel engine. In: *Thermo- and fluid-dynamic processes in diesel engines (THIESEL 2014)*, Valencia, Spain, 2014.
31. Moon S, Huang W, Li Z, et al. End-of-injection fuel dribble of multi-hole diesel injector: comprehensive investigation of phenomenon and discussion on control strategy. *Appl Energy* 2016; 179: 7–16.
32. Hélie J, Lamarque N, Fremaux J-L, et al. The process of tip wetting at the spray injection end. *Int J Engine Res* 2019; 22(1): 125–139.
33. Sechenyh V, Duke DJ, Swantek AB, et al. Quantitative analysis of dribble volumes and rates using three-dimensional reconstruction of X-ray and diffused back-illumination images of diesel sprays. *Int J Engine Res* 2020; 21: 43–54.
34. Battistoni M, Kastengren AL, Powell CF, et al. Fluid dynamics modeling of end-of-injection process. In: *26th annual conference on liquid atomization and spray systems (ILASS 2014)*, Portland, OR, 2014.
35. Mouvanal S, Burkhardt A, Bakshi S, et al. Numerical study of purging of a gasoline direct injection nozzle at the end of injection. *Int J Engine Res*. Epub ahead of print 4 May 2020. DOI: 10.1177/1468087420916658.
36. Örley F, Hickel S, Schmidt SJ, et al. Large-Eddy Simulation of turbulent, cavitating fuel flow inside a 9-hole diesel injector including needle movement. *Int J Engine Res* 2016; 18(3): 195–211.
37. Chiavola O and Palmieri F. Modeling needle motion influence on nozzle flow in high pressure injection system. SAE technical papers 2007-01-0250, 2007.
38. Spathopoulou M, Papoulias D, Giannadakis E, et al. Influence of the spatially resolved nozzle hole exit flow distribution on diesel spray development. SAE technical papers 2007-24-0025, 2007, 10.4271/2007-24-0025.
39. Gomez Santos E, Shi J, Gavaises M, et al. Investigation of cavitation and air entrainment during pilot injection in real-size multi-hole diesel nozzles. *Fuel* 2020; 263: 116746.
40. Jadidbonab H, Mitroglou N, Karathanassis I, et al. Experimental study of diesel-fuel droplet impact on a similarly sized polished spherical heated solid particle. *Langmuir* 2018; 34: 36–49.
41. Jadidbonab H, Malgarinos I, Karathanassis I, et al. We-T classification of diesel fuel droplet impact regimes. *Proc R Soc A Math Phys Eng Sci* 2018; 474: 20170759. 2018.
42. Strotos G, Malgarinos I, Nikolopoulos N, et al. Predicting the evaporation rate of stationary droplets with the VOF methodology for a wide range of ambient temperature conditions. *Int J Therm Sci* 2016; 109: 253–262.
43. Strotos G, Aleksis G, Gavaises M, et al. Non-dimensionalisation parameters for predicting the cooling effectiveness of droplets impinging on moderate temperature solid surfaces. *Int J Therm Sci* 2011; 50: 698–711.
44. Kim Y-J, Choi J, Son SU, et al. Comparative study on ejection phenomena of droplets from electro-hydrodynamic jet by hydrophobic and hydrophilic coatings of nozzles. *Jpn J Appl Phys* 2010; 49: 060217.
45. Bishnoi P and Sinha M. Influence of the wettability nature of the nozzle wall on the dynamics of drop formation. *Int J Heat Technol* 2018; 36: 1005–1009.
46. Fukai J, Shiiba Y, Yamamoto T, et al. Wetting effects on the spreading of a liquid droplet colliding with a flat surface: experiment and modeling. *Phys Fluids* 1995; 7: 236–247.
47. Brackbill JU, Kothe DB and Zemach CJ. A continuum method for modeling surface tension. *Comput Phys* 1992; 100: 335–354.
48. Sui Y, Ding H and Spelt PDM. Numerical simulations of flows with moving contact lines. *Annu Rev Fluid Mech* 2014; 46: 97–119. DOI: 10.1146/annurev-fluid-010313-141338.
49. Malgarinos I, Nikolopoulos N, Marengo M, et al. VOF simulations of the contact angle dynamics during the drop spreading: standard models and a new wetting force model. *Adv Colloid Interface Sci* 2014; 212: 1–20.
50. Mithun MG, Koukouvnis P, Karathanassis IK, et al. Simulating the effect of in-nozzle cavitation on liquid atomisation using a three-phase model. In: Katz J (ed.) *Proceedings of the 10th international symposium on cavitation (CAV2018)*., Baltimore, USA, 2018. New York, NY: ASME.
51. Mithun M-G, Koukouvinis P, Karathanassis IK, et al. Numerical simulation of three-phase flow in an external gear pump using immersed boundary approach. *Appl Math Modell* 2019; 72: 682–699.
52. Koukouvinis P, Bruecker C and Gavaises M. Unveiling the physical mechanism behind pistol shrimp cavitation. *Sci Rep* 2017; 7: 13994.
53. Manin J, Pickett LM and Yasutomi K. Transient cavitation in transparent diesel injectors. In: *ICLASS 14th triennial international conference on liquid atomization and spray systems*, Chicago, USA, 2018.
54. Menter FR. Two-equation eddy-viscosity turbulence models for engineering applications. *AIAA J* 1994; 32: 1598–1605.
55. Ansys. *Ansys Fluent Theory Guide*, Release 18.1. Ansys Inc. 2017.
56. Ubbink O. *Numerical prediction of two fluid systems with sharp interfaces*. Imperial College of Science, Technology and Medicine, London, 1997.
57. Peskin CS. Flow patterns around heart valves: a numerical method. *J Comput Phys* 1972; 10: 252–271.
58. Koukouvinis P, Mitroglou N, Gavaises M, et al. Quantitative predictions of cavitation presence and erosion-prone locations in a high-pressure cavitation test rig. *J Fluid Mech* 2017; 819: 21–57.
59. Koukouvinis P, Naseri H and Gavaises M. Performance of turbulence and cavitation models in prediction of incipient and developed cavitation. *Int J Engine Res* 2017; 18: 333–350.
60. Koukouvinis P, Vidal-Roncero A, Rodriguez C, et al. High pressure/high temperature multiphase simulations of dodecane injection to nitrogen: application on ECN Spray-A. *Fuel* 2020; 275: 117871.

61. Gavaises M, Arcoumanis C, Roth H, et al. Nozzle flow and spray characteristics from VCO diesel injector nozzles. In: *Thermo- and fluid dynamic processes in diesel engines* 2, 2004, pp. 31–48. Berlin, Heidelberg: Springer Berlin Heidelberg.
62. Cristofaro M, Edelbauer W, Koukouvinis P, et al. A numerical study on the effect of cavitation erosion in a diesel injector. *Appl Math Modell* 2020; 78: 200–216.
63. Cristofaro M, Edelbauer W, Koukouvinis P, et al. Influence of diesel fuel viscosity on cavitating throttle flow simulations under erosive operation conditions. *ACS Omega* 2020; 5: 7182–7192.
64. Caupin F and Stroock AD. The stability limit and other open questions on water at negative pressure. *Adv Chem Phys* 2013; 152: 51–80.
65. Trevena DH. Cavitation and the generation of tension in liquids. *J Phys D Appl Phys* 1984; 17: 2139–2164.
66. Schnerr GH and Sauer J. Physical and numerical modeling of unsteady cavitation dynamics. In: *Fourth international conference on multiphase flow*, New Orleans, LA, USA, 2001.
67. Singhal AK, Athavale MM, Li H, et al. Mathematical basis and validation of the full cavitation model. *J Fluids Eng* 2002; 124: 617.
68. Zwart PJ, Gerber AG and Belamri T. A two-phase flow model for predicting cavitation dynamics. In: *ICMF 2004 international conference on multiphase flow*, Yokohama, Japan, 2004.
69. Naseri H, Trickett K, Mitroglou N, et al. Turbulence and cavitation suppression by quaternary ammonium salt additives. *Sci Rep* 2018; 8: 7636.
70. Kedrinskiy VK. *Hydrodynamics of explosion*. Berlin/Heidelberg: Springer-Verlag.
71. Koukouvinis P and Gavaises M. Simulation of throttle flow with two phase and single phase homogenous equilibrium model. *J Phys Conf Ser* 2015; 656: 1–4.
72. Theodorakakos A, Mitroglou N and Gavaises M. Simulation of heating effects caused by extreme fuel pressurisation in cavitating flows through diesel fuel injectors. In: *Proceedings of the 8th international symposium on cavitation (CAV2012)*, Singapore, 2012, pp. 520–526. Singapore: Research Publishing Services.
73. Theodorakakos A, Mitroglou N and Gavaises M. Simulation of heating effects caused by fuel pressurisation at 3000 bar in diesel fuel injectors. In: *11th engine combustion processes*, Ludwigsburg, Germany, 2013.
74. George S, Phoevos K, Andreas T, et al. Quantification of friction-induced heating in tapered diesel orifices. In: *SIA international conference on diesel powertrains*, Rouen, France, 2014.
75. Strotos G, Koukouvinis P, Theodorakakos A, et al. Fuel heating in high pressure diesel nozzles. In: *Conference on thermo- and fluid-dynamic processes in diesel engines (THIESEL 2014)*, Valencia, Spain, 2014.
76. Salemi R, Koukouvinis P, Strotos G, et al. Evaluation of friction heating in cavitating high pressure Diesel injector nozzles. In: *Proceedings of the 9th international symposium on cavitation, (CAV2015)*, Lausanne, Switzerland, 2015.
77. Theodorakakos A, Strotos G, Mitroglou N, et al. Friction-induced heating in nozzle hole micro-channels under extreme fuel pressurisation. *Fuel* 2014; 123: 143–150.
78. Salemi R, McDavid R, Koukouvinis P, et al. Steady state and transient, non-isothermal modeling of cavitation in diesel fuel injectors. In: *27th annual conference on liquid atomization and spray systems (ILASS Americas)*. Raleigh, NC, 2015.
79. Strotos G, Koukouvinis P, Theodorakakos A, et al. Transient heating effects in high pressure Diesel injector nozzles. *Int J Heat Fluid Flow* 2015; 51: 257–267.
80. Rokni HB, Gupta A, Moore JD, et al. Purely predictive method for density, compressibility, and expansivity for hydrocarbon mixtures and diesel and jet fuels up to high temperatures and pressures. *Fuel* 2019; 236: 1377–1390.
81. Rokni HB, Moore JD, Gupta A, McHugh MA and Gavaises M. Entropy scaling based viscosity predictions for hydrocarbon mixtures and diesel fuels up to extreme conditions. *Fuel* 2019; 241: 1203–1213. 2019.
82. Rokni HB, Moore JD, Gupta A, et al. General method for prediction of thermal conductivity for well-characterized hydrocarbon mixtures and fuels up to extreme conditions using entropy scaling. *Fuel* 2019; 245: 594–604.
83. Arcoumanis C, Gavaises M, Nouri JM, et al. Analysis of the flow in the nozzle of a vertical multi-hole diesel engine injector. SAE technical papers 980811, 1998.
84. Arcoumanis C, Flora H, Gavaises M, et al. Cavitation in real-size multi-hole diesel injector nozzles. SAE technical papers 2000-01-1249, 2000.
85. Gavaises M, Andriotis A, Papoulias D, et al. Characterization of string cavitation in large-scale Diesel nozzles with tapered holes. *Phys Fluids* 2009; 21: 052107.